nature astronomy

Article

https://doi.org/10.1038/s41550-025-02621-8

Constraints on axion-like particles from active galactic nuclei seen through galaxy clusters

Received: 17 September 2024

Accepted: 30 June 2025

Published online: 15 August 2025

Check for updates

Denys Malyshev [1] ✉, Lidiia Zadorozhna [2,3], Yuriy Bidasyuk [4], Andrea Santangelo [1] & Oleg Ruchayskiy [2] ✉

Hypothetical axion-like particles (ALPs) are of interest because of their potential to act as dark matter or to reveal information about yet undiscovered fundamental constituents of matter. Such particles may be created when photons traverse regions of magnetic fields. The conversion probability depends on both the magnetic field parameters and the photon energy, leading to several spectral absorption features as light passes through magnetized regions. Traditionally, astrophysical searches have focused on detecting such features in individual objects. However, our limited understanding of the properties of cosmic magnetic fields has hindered progress. Here we introduce a new approach based on analysing the stacked (rather than individual) spectra of active galactic nuclei behind galaxy clusters, which are gigantic magnetic field reservoirs. Stacking efficiently averages over the uncertainties in magnetic fields, predicting a distinct step-like spectral signature of photon-to-ALP conversion. With this approach, we advance into previously inaccessible regions of the ALP parameter space for nano-electronvolt masses. Adopting this method using data from different telescopes and increasing the size of the stacked datasets will significantly improve existing bounds across a wide range of masses. The Cherenkov Telescope Array Observatory will enable this method to probe a broad region of parameter space where ALPs could serve as dark matter.

Cosmic environments provide unique physical conditions (densities, temperatures, and spatial and temporal scales) unattainable in terrestrial experiments. Consequently, astrophysical sites can serve as alternative laboratories for particle physics. In particular, they offer unique opportunities to study hypothetical particles that interact minimally with known forms of matter[1]. Extreme astrophysical conditions may facilitate the production of these particles. Thus, their presence could be deduced from astronomical observations.

Many extensions of the Standard Model of particle physics predict the existence of new, currently undetected particles. These extensions are motivated by observational challenges, such as the existence of dark matter and the absence of primordial antimatter in the Universe, and by quests to understand the underlying structure of physical theories. See refs. 2–4 for a review.

Axions are prime examples of such particles. Originally postulated in an attempt to solve the so-called strong-CP problem—a mysterious cancellation between two seemingly unrelated contributions, leading to the absence of charge-plus-parity violation in strong interactions[5,6]—they were quickly recognized as promising dark matter candidates[7,8]. The subsequent development of the idea led to a broader concept of

[1]Institut für Astronomie und Astrophysik Tübingen, Universität Tübingen, Tübingen, Germany. [2]Niels Bohr Institute, University of Copenhagen, Copenhagen, Denmark. [3]Taras Shevchenko National University of Kyiv, Kyiv, Ukraine. [4]Bogolyubov Institute for Theoretical Physics of the National Academy of Sciences of Ukraine, Kyiv, Ukraine. ✉e-mail: denys.malyshev@astro.uni-tuebingen.de; Oleg.Ruchayskiy@nbi.ku.dk

 https://doi.org/10.1038/s41550-025-02621-8

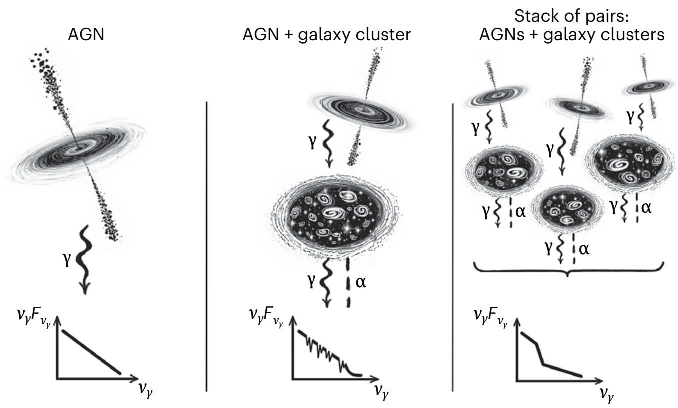

Fig. 1 | Illustration of how stacking spectra reveals information about photon-to-ALP conversion. Left: AGNs have featureless spectra of γ-ray emission. If ALPs exist in nature, some of the AGN photons will be converted to ALPs while passing through galaxy clusters that are large reservoirs of magnetic fields. Such a photon-to-ALP conversion creates a set of absorption features in the AGN spectra. Centre: for each particular AGN, these features cannot be predicted due to the lack of detailed knowledge about the magnetic field in individual clusters. Right: by stacking many observational pairs (AGNs plus clusters), the overall absorption feature becomes regularly shaped. ν_γ, photon frequency; $F_{\nu\gamma}$, spectral flux density.

axion-like particles (ALPs), which are light pseudo-scalar bosons with mass m_a whose interaction with electromagnetic fields is governed by

$$\mathcal{L}_{\rm int} = g_{a\gamma}\mathbf{E}\cdot\mathbf{B}\,a. \quad (1)$$

Here a is the ALP field, and **E** and **B** are the electric and magnetic fields, respectively (Methods). The unknown ALP–photon coupling constant $g_{a\gamma}$ characterizes the strength of the interaction and is measured in gigaelectronvolts.

The interaction term given by equation (1) causes energy-dependent photon-to-ALP conversions when photons traverse regions with strong or large-scale magnetic fields[1]. Specifically, as photons emitted by an astrophysical object pass through such regions, photon-to-ALP conversion results in spectral irregularities (for example, several absorption features) in the observed emission. The detection of these features in the otherwise smooth spectra of astrophysical objects would be a smoking gun for the existence of ALPs. This approach thus offers a compelling method for identifying ALPs and highlights astrophysical sites like neutron stars[9,10], white dwarfs[11,12], active galactic nuclei (AGNs)[13], supernovae[14–17] and clusters of galaxies[18–21] as prime laboratories for ALP searches.

The search for ALP-induced absorption features in individual bright astrophysical sources typically uses a statistical approach to detect spectral irregularities. The specific characteristics of these spectral features are determined by the exact distribution of the intervening magnetic field. Even minor variations in the orientation, spatial distribution or strength of the magnetic field affect the photon-to-ALP conversion probability in a quasi-random way, as illustrated in Figs. 1 and 2. To address the substantial uncertainties and poor knowledge about the magnetic fields, existing methods, therefore, require marginalizing over a large number of potential realizations of random magnetic fields within a selected object[20–31]. Therefore, the improvement of astrophysical bounds on ALP couplings has been hindered by the challenge of accounting for all the unknowns.

Stacked analysis

In this work, we explore a distinctly different approach (Fig. 1). Rather than focusing on individual bright sources of photons and marginalizing over the details of the magnetic field distribution within these objects, we exploit the power of ensemble averaging over a large number of sources. Figure 2 illustrates this approach. The blue curves show the survival probability of a photon as it traverses a region of the magnetic field (for example, a galaxy cluster), with each curve representing a different realization of the field. This probability (and the resulting absorption features in the observed spectrum) has a complex shape, with little similarity between different realizations. However, the averages over a large number of such curves (shown as black lines) are much smoother and show apparent similarities. Moreover, the black curves exhibit a distinct, realization-independent spectral signature—a step-like suppression at high energies—which serves as a clear indicator for ALP searches. This makes studying photon-to-ALP conversion in a stacked set of clusters substantially simpler than conducting searches in individual objects.

References [24,32,33] have previously put constraints on ALPs using several extragalactic objects. Our approach introduces a key distinction: by averaging over previously unknown parameters—the magnetic fields in galaxy clusters—we effectively reduce the inherent uncertainties, making the sought-after signal predictable.

To implement this idea, we stack the spectra of γ-ray-bright AGNs behind galaxy clusters. AGNs have smooth spectra in the giga-electronvolt energy range, and galaxy clusters serve as vast reservoirs of magnetic fields. Consequently, photon-to-ALP conversion may occur, leading to a suppression of the high-energy portions of AGN spectra.

Main steps of the data analysis

Using the most recent Fermi Large Area Telescope (Fermi/LAT) catalogue[34,35] and galaxy cluster catalogues[36–38], we identified 32 AGNs that are located behind known galaxy clusters (Extended Data Table 1). The selection procedure is detailed in Methods. We fit each AGN spectrum with a log-parabola (smooth 3 parametric function, known to describe well the AGN γ-spectra[39]). We also account for the

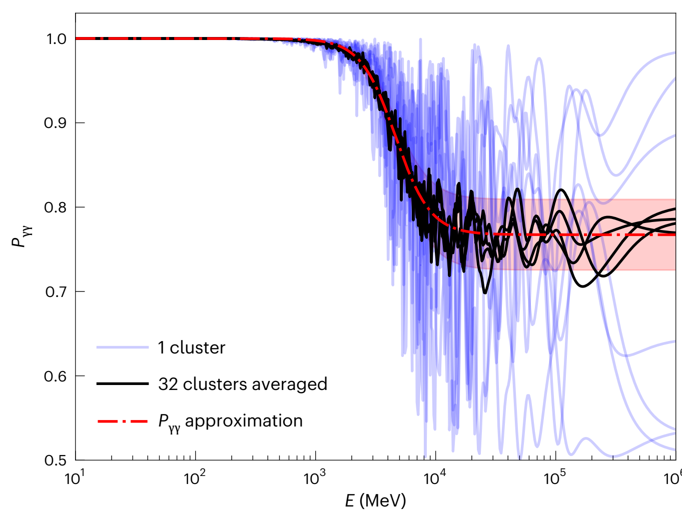

Fig. 2 | Photon survival probability and its averages. Photon survival probability ($P_{\gamma\gamma}$) when passing through one galaxy cluster for different realizations of the cluster magnetic field (blue lines). All realizations have a magnetic field with the same radial profile, but they vary randomly in their orientation in the photon polarization plane and in the sizes of the domains where the field remains approximately constant. Black lines demonstrate the effect of averaging over 32 randomly selected realizations. The red dotted-dashed line shows the analytical approximation to these lines, given by equation (2) with parameters p_0 = 0.23, E_c = 5.5 GeV and k = 3.14. The red-shaded region represents the systematic uncertainty due to the finite number of sources used in our analysis. The ALP parameters for all curves are (m_a, $g_{a\gamma}$) = (3 neV, 2×10^{-12} GeV^{-1}). Blue curves were obtained by numerically solving the ALP propagation equations with the ALPro code[31,59].

 https://doi.org/10.1038/s41550-025-02621-8

interaction of γ-ray photons with extragalactic background light (EBL), which produces electron–positron pairs. Such an interaction leads to the suppression of the high-energy part of the AGN spectrum, partially mimicking the effect of photon-to-ALP conversion. The suppression is a function of the AGN redshift only and does not increase the number of fitting parameters. This fit is our baseline model.

Subsequently, we repeat the spectral analysis by multiplying each of the above functions by a common smooth function (red line in Fig. 2):

$$P_{\gamma\gamma} \equiv 1 - \langle P_{\gamma a}(E) \rangle = 1 - \frac{p_0}{1 + (E_c/E)^k}. \quad (2)$$

Here p_0 represents the suppression depth at high energies, E_c denotes the characteristic transition energy and k determines the sharpness of the transition; all three parameters are functions of m_a and $g_{a\gamma}$, as Extended Data Fig. 1 illustrates. By demanding that the resulting χ^2 of the fit worsens by $\Delta\chi^2 \geq 6.2$, we draw the 95% confidence level contours in the plane $(m_a, g_{a\gamma})$, thus excluding ALPs with the corresponding parameters.

Results

The green solid line in Fig. 3 defines the excluded region of ALP parameters and represents our main result. We have strengthened the existing constraints[40] by up to a factor of 4 for ALP masses in the range 1 to 10 neV. In deriving this bound, we assumed that all clusters in our sample have magnetic fields like that of the Coma cluster. The green-shaded area around the line reflects how the uncertainty in both the magnitude and spatial distribution of the magnetic field of the Coma cluster propagates to the ALP bounds. The blue dashed-dotted line represents an alternative scenario where the magnetic field strength correlates with cluster mass, as indicated by some numerical simulations[41]. However, existing observations do not support such a scaling[42–44]. See Methods and Extended Data Fig. 2 for details. Therefore, we consider this scenario overly pessimistic.

These results take into account systematic uncertainties arising from the imprecise knowledge of the Fermi/LAT effective area. Following the collaboration guidelines (see the Fermi/LAT website: https://fermi.gsfc.nasa.gov/ssc/data/analysis/scitools/AeffSystematics.html), we assume energy-dependent systematics ranging from 3% to 10%. We allow p_0 and E_c to vary by 20% and 12%, respectively, to account for the finite sample size, and we treat these uncertainties as 1σ errors (Extended Data Fig. 3). For comparison, we also present a purely statistical bound (the dotted line), derived without including such systematic uncertainty. In this case, the constraints on $g_{a\gamma}$ improve the existing bounds by up to a factor of 7.5. The improved bounds extend into the region of the parameter space where ALP particles could potentially serve as dark matter candidates[45].

Intriguingly, a second disjoint exclusion region appears in this case. Between the two regions, the ALP actually improves the fit quality, indicating a marginal detection at approximately the 2σ level (Extended Data Fig. 4). The shape of this region follows a $g_{a\gamma} \propto m_a^2$ relation, which maintains a constant characteristic energy E_c in equation (2) (Extended Data Fig. 1). Although most AGN spectra exhibit a consistent improvement in fit quality when the characteristic energy is around $E_c \approx 600$ MeV, two objects (NGC 1275 and 4FGL J0038.2-2459 (PKS0035-252)) show the most pronounced effect (Extended Data Table 2). Given the limited sample size and low statistical significance, however, it is too early to draw firm conclusions regarding this potential detection. Note that the ALP parameters that show the maximal $\Delta\chi^2$ improvement are in the region of parameter space where the existence of such particles has previously been suggested based on tera-electronvolt transparency arguments[46] and stellar evolution studies[47].

Future improvements

In this work, we put forward a new method of searching for ALPs based on using the stacked spectra of AGNs behind galaxy clusters. Collectively fitting many spectra allows us to search for a regular step-like suppression feature rather than for irregular photon transparency in individual clusters. The uncertainties related to the unknown characteristics and distribution of magnetic fields in individual galaxy clusters are reduced to essentially one number—the average magnetic field across the sample (Extended Data Fig. 3 and Supplementary Information).

Our method not only proposes the most competitive constraints but also shows a great potential for improvement. The observations of a similar number of sources at other wavelengths with current or future missions, for example, at kilo-electronvolt energies with Swift, at mega-electronvolt energies with the All-sky Medium Energy Gamma-ray Observatory and GECCO, and at tera-electronvolt energies with the Cherenkov Telescope Array Observatory (CTAO)[48,49], would result in a substantial extension of the derived limits to lower and higher ALP masses. This is illustrated by the red dashed line in Fig. 3, which shows the potential reach of similar searches performed with the CTAO. Different energy ranges of the CTAO open access to larger ALP masses and promise an order of magnitude improvement in $g_{a\gamma}$. In particular, such searches will explore a part of the ALP dark matter parameter space.

The current analysis is based on only 32 AGN–cluster pairs. Further progress (Extended Data Fig. 5) will be achieved as more galaxy clusters are detected due to the Sunyaev–Zeldovich effect with present-day X-ray all-sky surveys, such as eROSITA[50]. Further significant advances will come from all-sky polarization radio surveys, such as those planned with the Square Kilometre Array, which will greatly expand the number of galaxy clusters detected and enhance our understanding of intracluster magnetic fields[51,52].

Future studies should also address several aspects beyond this proof-of-concept work. These include a more detailed investigation of

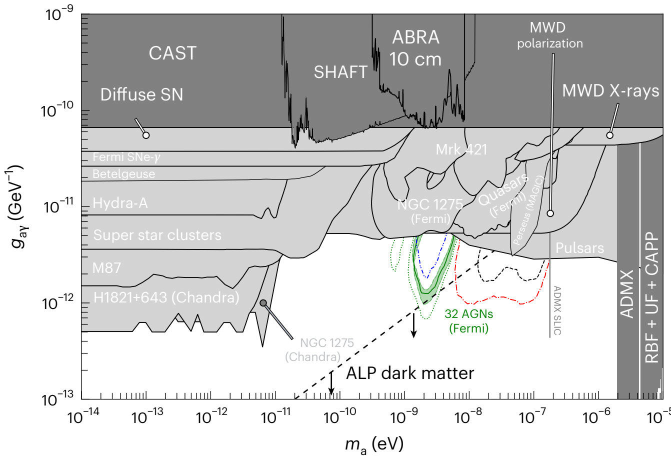

Fig. 3 | ALP–photon coupling constraints from AGN–cluster pairs. The green solid curve represents the 95% upper limits on the coupling $g_{a\gamma}$ derived from the stacked analysis of the spectra of AGNs behind galaxy clusters and based on our estimate of the average magnetic field across the sample. The green-shaded region surrounding this curve indicates the uncertainty in the field estimate. The blue dashed-dotted line illustrates a pessimistic scenario where the magnetic field weakens with decreasing cluster mass. The green dotted line shows constraints based solely on statistical errors. Between the two disjoint regions, the quality of fit improves by up to 2σ when including an ALP. The red dotted-dashed line highlights potential improvements achievable with the CTAO using the same AGN–cluster pairs. Grey regions display existing exclusion bounds from ref. 40. SN, supernova; SNe, supernovae. CAST, CERN Axion Solar Telescope; SHAFT, the Search for Halo Axions with Ferromagnetic Toroids; ABRACADABRA, A Broadband/Resonant Approach to Cosmic Axion Detection with an Amplifying B-field Ring Apparatus (ABRA); MWD, magnetic white dwarf; ADMX, Axion Dark Matter Experiment; ADMX SLIC, Superconducting LC Circuit Investigating Cold Axions; RBG, Rochester–Brookhaven–Fermilab; UF, University of Florida; CAPP, Center for Axion and Precision Physics Research.

magnetic field distributions in galaxy clusters and the development of a physically motivated model for background AGN emission. We also note that constraining the average magnetic field properties across a large sample of clusters may be more tractable than modelling the magnetic field of an individual cluster in detail.

Methods

ALP propagation equations

In this section, we summarize the key theoretical ingredients relevant to the studies of ALPs and photon-to-ALP conversion in external magnetic fields. An extensive review of the subject can be found in, for example, ref. 53.

The interactions of ALPs with an electromagnetic field are governed by the following Lagrangian:

$$\mathcal{L} = -\frac{1}{4}F_{\mu\nu}F^{\mu\nu} + \frac{1}{2}\left(\partial_\mu a \partial^\mu a - m_a^2 a^2\right) + \frac{1}{4}g_{a\gamma}F_{\mu\nu}\tilde{F}^{\mu\nu}\, a. \qquad (3)$$

Here a is the ALP field, m_a is its mass, $F_{\mu\nu}$ is the electromagnetic field strength tensor and $\tilde{F}_{\mu\nu} \equiv \frac{1}{2}\varepsilon_{\mu\nu\rho\sigma}F^{\rho\sigma}$ is the electromagnetic dual tensor, where $\epsilon_{\mu\nu}$ is the totally antisymmetric tensor in 4D (Levi–Civita tensor). The photon–ALP coupling constant $g_{a\gamma}$ characterizes the interaction strength. The coupling between ALPs and electromagnetic fields, described by the third term in equation (3), can be expressed as in equation (1). We use natural Lorentz–Heaviside units with $\hbar = c = k_B = 1$, where $\hbar$ is the reduced Planck constant, c the speed of light and k_B the Boltzmann constant. The fine-structure constant $\alpha = e^2/4\pi \approx 1/137$, where e is the electron charge.

The Lagrangian in equation (3) indicates that a photon can convert into an ALP when passing through a magnetic field[11]. To derive the relevant formulas, consider a photon with energy E propagating through the magnetic field in the z direction. The component of the magnetic field perpendicular to the propagation direction is denoted by $\mathbf{B}_\perp = \mathbf{B} - B_z\mathbf{e}_z$, where $\mathbf{e}_z$ is a unit vector in the z direction. The joint evolution of the perpendicular photon components (A_x, A_y) and ALP a are described by the equation[11,26,54]

$$\left[E - \mathrm{i}\frac{\partial}{\partial z} - \mathcal{M}(m_a, g_{a\gamma}, \mathbf{B}_\perp(z))\right]\begin{pmatrix} A_x \\ A_y \\ a \end{pmatrix} = 0, \qquad (4)$$

where the mixing matrix $\mathcal{M}(m_a, g_{a\gamma}, \mathbf{B}_\perp(z))$ depends on the strength and orientation of the magnetic field, the ALP mass m_a and the coupling constant $g_{a\gamma}$. For mega- to giga-electronvolt photon energies and typical microgauss-scale intracluster magnetic fields, the cosmic microwave background term[55] and the quantum electrodynamics term[11] are negligible, so the matrix $\mathcal{M}$ is given by:

$$\mathcal{M} = \begin{pmatrix} 0 & 0 & \Delta_{a\gamma}\cos\phi \\ 0 & 0 & \Delta_{a\gamma}\sin\phi \\ \Delta_{a\gamma}\cos\phi & \Delta_{a\gamma}\sin\phi & \Delta_a \end{pmatrix}, \qquad (5)$$

where $\cos\phi = \mathbf{B}_\perp \cdot \mathbf{e}_x / B_\perp = \sqrt{1-\sin^2\phi}$ and

$$\Delta_a = -\frac{m_a^2}{2E} \approx -7.04\times10^{-4}\left(\frac{m_a}{3\times10^{-9}\,\mathrm{eV}}\right)^2\left(\frac{E}{1\,\mathrm{GeV}}\right)^{-1}\mathrm{pc}^{-1},$$
$$\Delta_{a\gamma} = \frac{1}{2}g_{a\gamma}B_\perp \approx 3.05\times10^{-6}\left(\frac{g_{a\gamma}}{2\times10^{-12}\mathrm{GeV}^{-1}}\right)\left(\frac{B_\perp}{1\,\mu\mathrm{G}}\right)\mathrm{pc}^{-1}. \qquad (6)$$

For lower energies, the plasma frequency of the galaxy clusters and the possibility of resonant photon-to-ALP conversion should be taken into account; see, for example, refs. 56,57. It is instructive to solve equation (4) for the scenario where a photon propagates through a region with a constant magnetic field. The probability of photon-to-ALP conversion is energy-dependent, and after travelling a distance l, it is given by[11]:

$$P_{\gamma a} \approx \frac{(\Delta_{a\gamma}l)^2}{(\Delta_{\mathrm{osc}}l/2)^2}\sin^2\left(\frac{\Delta_{\mathrm{osc}}\,l}{2}\right). \qquad (7)$$

Here the oscillation wavenumber Δ_{osc} is given by

$$\Delta_{\mathrm{osc}} \approx \left[\Delta_a^2 + 4\Delta_{a\gamma}^2\right]^{1/2} = 2\Delta_{a\gamma}\sqrt{1+\left(\frac{E_c}{E}\right)^2}, \qquad (8)$$

and E_c represents the characteristic energy of oscillations in $P_{\gamma a}$:

$$E_c \equiv E\frac{\Delta_a}{2\Delta_{a\gamma}} \approx 115\,\mathrm{GeV}\left(\frac{m_a}{3\,\mathrm{neV}}\right)^2\left(\frac{B_\perp}{1\,\mu\mathrm{G}}\right)^{-1}\left(\frac{g_{a\gamma}}{2\times10^{-12}\mathrm{GeV}^{-1}}\right)^{-1}. \qquad (9)$$

Conversion probability averaged across many domains and objects

The above formulas are for an idealized set-up of photon-to-ALP conversion in a constant magnetic field. More relevant for our discussion is the case when the field changes along the trajectory of the photon. To wit, consider N domains of size l, with the amplitude of the magnetic field being the same in each of them. The conversion probability in a single domain $P_{\gamma a}$ is given by equation (7). It can be shown[16,23,56,58] that by crossing $N \gg 1$ domains and averaging over the orientations of the magnetic field across many similar objects, the conversion probability simplifies to

$$\langle P_{\gamma a}\rangle \approx \frac{1}{3}\left(1 - \mathrm{e}^{-3NP_{\gamma a}/2}\right). \qquad (10)$$

Thus defined, $\langle P_{\gamma a}\rangle$ is a step-like function of the photon energy E. Although at low energies ($E \ll E_c$), we have $\langle P_{\gamma a}\rangle \approx 0$, it saturates to a constant at $E \gg E_c$ with a saturation level proportional to $g_{a\gamma}$ for $\langle P_{\gamma a}\rangle \ll 1/3$ and asymptotically reaching 1/3 with an increase of $g_{a\gamma}$.

The $\langle\ldots\rangle$ symbol stresses that this result appears only after averaging over many objects. Without such averaging, we would not obtain a step-like suppression (corresponding to the black curves in Fig. 2) but rather have the random blue curve.

Photon-to-ALP conversion in the inhomogeneous magnetic field of galaxy clusters

Finally, we describe how we obtained the expression $\langle P_{\gamma a}\rangle$ when not only the orientation but also the amplitude of the magnetic field changes along the line of sight. For the magnetic field of a cluster with a realistic spatial profile, we solved equation (4) numerically using the ALPro code[31,59] in the 'custom model' mode. This mode accepts as an input the list of magnetic field magnitudes and orientations in a set of domains along the trajectory of the light. Within each of these domains, the strength and the orientation of the magnetic field are constant. We assumed that the strength of the magnetic field in each cluster is proportional to the density of plasma electrons and depends only on the distance to the centre of the cluster r:

$$B(r) = B_0[n_e(r)/n_0]^\eta, \qquad (11)$$

where $B(r)$ is the amplitude of the magnetic field, $B(r) = |\mathbf{B}(r)|$. The parameters in equation (11) were adopted from those of the Coma cluster, the only galaxy cluster for which the strength profile of the magnetic field has been determined fairly well[60,61]. The density of electrons n_e is described by the β-model, $n_e(r)/n_0 = [1+(r/r_c)_2]^{-3\beta/2}$ with $n_0 = 3.44\times10^{-3}\,\mathrm{cm}^{-3}$, $\beta = 0.75$ and $r_c = 291$ kpc (refs. 61,62). The values of $(B_0, \eta) = (5.2\,\mu\mathrm{G}, 0.67)$ were adopted from ref. 61. We note that adapting the parameters of the Perseus cluster from ref. 63 to model the contribution from NGC 1275 did not change the presented results.

The domain sizes were distributed randomly between 2 and 34 kpc, based on refs. 61,64. The cluster radius was set to 1.5 Mpc, as the substantial presence of the magnetic field at this distance has been reported in refs. 64,65. For each cluster, we performed 10^3 realizations of the magnetic field, randomly varying the orientation of the field in each domain and distributing the line-of-sight distance from the cluster centre randomly within 0 to 500 kpc. We confirmed that using actual distances instead of random distributions did not significantly affect the results.

For each realization of the magnetic field, we calculated $P_{\gamma a}(E)$ for a set of ALP parameters (m_a, $g_{a\gamma}$) (blue lines in Fig. 2). We averaged this function over the described realizations to obtain $\langle P_{\gamma a}(E)\rangle$, shown as the black lines in Fig. 2. This function is well approximated by equation (2) and is represented by the red line in the same figure. This procedure establishes a relation between the parameters (p_0, E_c, k) of the photon survival probability function $P_{\gamma\gamma} \equiv 1 - \langle P_{\gamma a}\rangle$ and the ALP parameters (m_a, $g_{a\gamma}$), shown in Extended Data Fig. 1.

As the ALP-to-photon conversion probability depends on the product of the magnetic field strength and the size of the region (equation (7)), we neglected the effects of the magnetic field of the Milky Way in our analysis. Although the magnetic field strengths in the Milky Way and galaxy clusters are comparable, the path length through galaxy clusters is larger by 1–2 orders of magnitude, making the cluster contribution dominant.

Dispersion of magnetic field strength

We repeated our analysis but spreading the values of β and η by up to ±90% around their adopted values. The characteristic energy E_c and the plateau height p_0 remained constant within 5%. Variations in the distribution of domain sizes had a negligible impact on the averaged curves.

As the photon-to-ALP conversion probability is directly proportional to the magnetic field value, we varied the parameter B_0 by an order of magnitude in each direction (from 0.52 μG to 52 μG). Extended Data Fig. 3 (left) shows that in this case, p_0 varies by about 20%, whereas the function $\langle P_{\gamma a}(E)\rangle$ maintained its shape, as given by equation (2). This demonstrates that averaging over clusters with significantly different magnetic field properties does not result in a conversion probability dominated by the extreme values within the distribution. Instead, the conversion probability is primarily governed by the average magnetic field strength across the sample of clusters.

Shifting the magnetic field amplitude

To estimate the potential impact of the change in the central value of B_0, we varied it from 3.1 μG to 6.5 μG. The values of B_0 and η are strongly correlated, with a smaller η corresponding to a smaller B_0. This correlation arises because the directly observed quantity is the rotation measure (RM):

$$\mathrm{RM} = 812 \int_{\mathrm{l.o.s.}} n_e B_{\parallel}\, \mathrm{d}\ell\ [\mathrm{rad\,m^{-2}}] \propto \frac{B_0}{3\beta(\eta+1)-1}. \quad (12)$$

The RM is sensitive to the mean value of the magnetic field along the line of sight (l.o.s.) and is measured with typically lower uncertainties than the derived parameters B_0 and η. Therefore, we accompanied a change in B_0 by changing the slope η between 0.4 and 0.7. Such a variation corresponds roughly to the 95% confidence level ranges reported for the Coma cluster[61]. The associated uncertainty is shown as the green-shaded region in Fig. 3. It amounts to a change in $g_{a\gamma}$ for a fixed m_a by about 20%.

Properties of the small-scale turbulent magnetic field

Equation (11) describes the radial dependence of the magnetic field amplitude. Within the spatial range defined by Λ_{min} and Λ_{max}, the magnetic field is turbulent, characterized by a power spectrum $|B_k|^2 \propto k^{-n}$. Typical values for Λ_{min} and Λ_{max} are illustrated in Extended Data Fig. 2a. For a further discussion, see ref. 66.

To reproduce the statistical properties of the turbulent magnetic field in numerical simulations of ALP propagation, the ALPro code samples domain sizes L from a power-law distribution $P(L) \propto L^{-a}$. For a Kolmogorov turbulence spectrum, the index was found[28] to be $a = 1/3$. We have explicitly adopted this value in our simulations, along with $\Lambda_{min} = 2$ kpc and $\Lambda_{max} = 34$ kpc, motivated by the corresponding values reported for the Coma cluster[28,61]. These parameters are representative of galaxy clusters, as Extended Data Fig. 2 illustrates. The choice of Λ_{max} lies on the lower end of the observed range of values. Given that the conversion probability scales as B^2l^2, with the turbulent magnetic field exhibiting greater power at larger scales, this choice represents a conservative estimate.

The value $n = 11/3$, corresponding to the Kolmogorov turbulent spectrum, is broadly consistent with observational data. However, the strong correlation among the parameters n, Λ_{min} and Λ_{max} (see, for example, ref. 67) complicates definitive conclusions about the universality of this value. Extended Data Fig. 2b highlights the variability in the values of n reported in the literature.

To account for the potential non-universality of the index n, we considered variations in the parameter a. Like other parameters, such as B_0 and η, the stacking procedure substantially reduces the scatter in the predicted photon-to-ALP conversion probabilities. The right panel of Extended Data Fig. 3 illustrates the conversion probability $P_{\gamma a}$ for specific values of a and for when a is drawn from a uniform distribution $0 \le a \le 1.2$, with the upper limit inferred from ref. 21. The figure demonstrates that, in the latter scenario representing the case of non-universality of the index a, the predicted value of p_0 would degrade by approximately 10%. This reduction remains well within the systematic uncertainty that we impose. Similarly, varying Λ_{min} and Λ_{max} by up to a factor of 2 resulted in only a negligible change in $P_{\gamma\gamma}$. Consequently, the derived constraints are insensitive to the exact values in individual clusters and instead depend on their average behaviour across the sample.

Along with the potential non-universality of global cluster-to-cluster turbulent characteristics, these properties can also vary within the same cluster as a function of the off-centre distance (see, for example, ref. 68) as well as due to local environmental effects, including cool cores, radio relics, merger-driven shocks and cold fronts. However, these features tend to increase the local value of the magnetic field (see, for example, refs. 69,70), meaning that our estimates remain conservative.

Average magnetic field strength across the sample of clusters

A crucial factor in our analysis is the estimate of the average magnetic field strength in our sample of galaxy clusters. This estimate could potentially be biased due to a correlation between the central magnetic field strength (B_0) and the cluster mass (M_{500}). The log-average mass of our sample is $M_{500} \approx 1.6 \times 10^{14}\, M_\odot$ (Extended Data Table 1), which is approximately four times smaller than $M_{500} \approx 6 \times 10^{14}\, M_\odot$, the mass of the Coma cluster[71].

Current observational data do not reveal any obvious correlation between B_0 and M_{500}, as Extended Data Fig. 2c illustrates. Moreover, different methods of evaluating the strength of the magnetic field (Faraday rotation, synchrotron diffuse radio emission and inverse Compton hard X-ray emission) provide different estimates of the magnetic field strength in clusters due to differences in measurement techniques, spatial scales and the complex structure of magnetic fields in cluster environments. See, for example, the discussion in refs. 44,72. Furthermore, an analysis comparing clusters with high and low temperatures revealed no significant variations in the RM data[73]. These findings, therefore, indicate the absence of a strong relation between the magnetic field and the cluster mass, given the well-established mass–temperature relation for clusters of galaxies; see, for example, ref. 74. Given this lack of a discernible trend, we argue that the magnetic field profile of the Coma cluster (with $B_0 \approx 5.2\ \mu$G) can be considered representative of our entire cluster sample.

Recent *N*-body simulations[41] indicate, however, a scaling relation $B_0 \approx M_{500}^{1/3}$. If this relation holds, the average B_0 in our sample would be approximately 1.6 times lower than in massive clusters like Coma. To assess the potential impact of this scaling on our results, we performed another analysis. We explicitly downscaled the magnetic field in our $\langle P_{\gamma a}(E)\rangle$ calculations based on the M_{500} masses of clusters in our sample (Extended Data Table 1) and the aforementioned scaling. The resulting limits on ALP parameters are shown as a blue dashed-dot-dotted line in Fig. 3. These limits are a factor of 1.6 weaker than those obtained using the characteristic magnetic field profile.

We note that the dependency of the central magnetic field on the redshift[41,75] of the clusters can be neglected, as the clusters are at low redshifts ($z_{GC} \lesssim 0.4$).

Correction for the finite sample size

To determine the relation between the parameters in equation (2) and the ALP parameters, we performed 200 simulations of $P_{\gamma\gamma}$ for each pair (m_a, $g_{a\gamma}$) and computed the average. The resulting values are presented in Extended Data Fig. 1. However, for our sample of 32 objects, relying solely on the central value of p_0 may overestimate the exclusion strength. Extended Data Fig. 5 illustrates how p_0 and E_c depend on the sample size. For our dataset, the dispersion in p_0 is 20%, whereas the variation in E_c is 12%, which is considerably smaller than the size of the Fermi/LAT energy bins. Notably, for this sample of 32 objects, the log-width of the distribution remains nearly constant across all (m_a, $g_{a\gamma}$) combinations. This consistency allowed us to adopt the same range of variations for p_0 and E_c for all ALP parameter sets that we use in deriving the bounds as described below.

Selection of AGN–cluster pairs

We identified γ-ray-bright AGNs located beyond or within known galaxy clusters based on the most recent catalogue of high-altitude ($|b| > 10°$) sources, 4LAC-DR3-h[76], and the catalogue of Sunyaev–Zeldovich, X-ray and optically identified galaxy clusters[36–38]. Among 1,806 AGNs with known redshifts and emission in the giga-electronvolt range and 47,600 clusters with known redshifts, we were able to identify 32 AGN–cluster pairs for which the line of sight to the AGN passes through the cluster at a comoving distance not exceeding R_{max} = 500 kpc (refs. 36,77) and $z_{AGN} \geq z_{GC}$. Note that the magnetic field typically continues to much larger radii, assumed to be 1.5 Mpc in this work in agreement with refs. 64,65. We additionally included in the sample two nearby AGNs (NGC 1275 and M87), located within the Perseus and Virgo clusters, respectively. The basic properties of the sample of AGNs and galaxy clusters are summarized in Extended Data Table 1.

Data and data analysis

The AGN spectra are provided by the Fermi/LAT collaboration as part of the 4FGL-DR4 catalogue[34,35] and correspond to 14-year time-averaged spectra. For each object from the selected sample, we considered its Fermi/LAT spectral energy distribution in eight energy bins, as reported in the 4FGL catalogue. We also assumed that, in addition to the statistical uncertainty, the spectral points are characterized by a certain level of systematic uncertainty (added in quadrature). We considered two choices of systematic uncertainty: (1) optimistic (systematic set to 0) and (2) 'nominal' (3% systematics at all energies except E < 100 MeV and E > 100 GeV, for which it was 10%). We present in this work the results for each of these choices.

We fitted the AGN spectra with the 'baseline' EBL-corrected log-parabola models:

$$\frac{dN}{dE} = N_0(E/E_0)^{-\alpha-\beta\log(E/E_0)} \times \kappa_{EBL}(E, z_{AGN}), \quad (13)$$

where the normalization N_0 and spectral parameters α and β are the free fitting parameters and E_0 = 1 GeV. The EBL-correction factor $\kappa_{EBL}(E, z)$ was calculated for AGN redshift z_{AGN} with the help of the absorption model provided within the naima Python module[78] based on the adopted EBL model[79].

Aiming to probe photon-to-ALP conversion as the AGN photons propagate through the clusters of galaxies, we considered an ALP model for a range of ALP masses and coupling constants:

$$\frac{dN}{dE} = N_0(E/E_0)^{-\alpha-\beta\log(E/E_0)} \times \kappa_{EBL}(E, z_{AGN})P_{\gamma\gamma}, \quad (14)$$

where $P_{\gamma\gamma}$ is given by equation (2). Three extra parameters of the function $P_{\gamma\gamma}$ (p_0, E_c, k) are related to the ALP parameters (m_a and $g_{a\gamma}$), as discussed above. The dependency of p_0 and E_c on the ALP parameters is shown in Extended Data Fig. 1.

The difference between the joint best-fitting χ^2 for the baseline model and ALP model is shown in Extended Data Fig. 4. In addition to the uncertainties for the spectral points discussed above, we allowed p_0 and E_c to vary by 20% and 12%, respectively, and treated these uncertainties as 1σ errors ('Correction for the finite sample size'). The green contours in this figure represent a deterioration in the fit with the ALP model by $\Delta\chi^2$ = 6.2 with respect to the baseline model, corresponding to a 2σ excluded region for two degrees of freedom. The green dotted line indicates the limits for the statistical-only uncertainty (0% systematics). The green solid line corresponds to the nominal Fermi/LAT systematics. The shaded region corresponds to the variations in the limits derived for the nominal level of Fermi/LAT systematics for the different profiles of the magnetic field of the Coma cluster (see above). The dashed-dotted region indicates the weakening of the limits when the magnetic field in each of the clusters in the sample is scaled with respect to the mass of the cluster, as discussed above. These same contours are depicted in Fig. 3.

The region bordered by the orange dotted-dashed line is where ALPs were detected with a $\gtrsim 2\sigma$ significance ($\Delta\chi^2 \leq -6.2$) in the absence of systematic uncertainty (purely statistical bound). The maximal improvement of the fit corresponds to $\Delta\chi^2 \approx -7.1$ for $m_a \approx 1$ neV and $g_{a\gamma} \approx 2 \times 10^{-12}$ GeV^{-1}. See Extended Data Table 2 for a summary of the $\Delta\chi^2$ improvement in individual objects. We note that this detection is not statistically significant and disappears in the presence of systematic uncertainties.

CTAO sensitivity

To estimate the sensitivity of the forthcoming tera-electronvolt CTAO for similar studies, we simulated a similar sample of 32 AGNs. We assumed that the AGN spectra continue as power laws in the energy band 0.03–10 TeV and that the CTAO will be able to measure eight spectral points in this energy band. We further assumed that the uncertainties of the flux measurements are dominated by 10% systematic uncertainties. We repeated the procedure described above for ALP searches in the simulated CTAO-only dataset. The estimated level of exclusions derived from such a dataset is shown with a red dot-dashed line in Fig. 3.

Data availability

The data from Fermi/LAT observations used in this paper were taken from the publicly available 4FGL-DR4 catalogue[35]. The AGN sample was taken from the catalogue of high-altitude ($|b| > 10°$) objects 4LAC-DR3-h[76] and the catalogue of clusters identified by the all-sky surveys 2MASS, WISE, Planck SZ, X-ray and SuperCOSMOS[36–38]. The catalogue names of the Fermi sources used in this paper can be found in Extended Data Tables 1 and 2.

Code availability

The ALP propagation code used in this study is the publicly available code ALPro (Axion-like Propagation)[31,59], available via GitHub at https://github.com/jhmatthews/alpro.

References

1. Raffelt, G. G. *Stars as Laboratories for Fundamental Physics: The Astrophysics of Neutrinos, Axions, and Other Weakly Interacting Particles* (Univ. Chicago Press, 1996).
2. Bertone, G., Hooper, D. & Silk, J. Particle dark matter: evidence, candidates and constraints. *Phys. Rep.* **405**, 279–390 (2005).
3. Rosenberg, L. J. & van Bibber, K. A. Searches for invisible axions. *Phys. Rep.* **325**, 1–39 (2000).
4. Chadha-Day, F., Ellis, J. & Marsh, D. J. E. Axion dark matter: what is it and why now? *Sci. Adv.* **8**, eabj3618 (2022).
5. Peccei, R. D. & Quinn, H. R. Constraints imposed by CP conservation in the presence of instantons. *Phys. Rev. D* **16**, 1791–1797 (1977).
6. Peccei, R. D. & Quinn, H. R. CP conservation in the presence of instantons. *Phys. Rev. Lett.* **38**, 1440–1443 (1977).
7. Wilczek, F. Problem of strong *P* and *T* invariance in the presence of instantons. *Phys. Rev. Lett.* **40**, 279–282 (1978).
8. Weinberg, S. A new light boson? *Phys. Rev. Lett.* **40**, 223–226 (1978).
9. Sedrakian, A. Axion cooling of neutron stars. *Phys. Rev. D* **93**, 065044 (2016).
10. Fiorillo, D. F. G. & Iocco, F. Axions from neutron star mergers. *Phys. Rev. D* **105**, 123007 (2022).
11. Raffelt, G. & Stodolsky, L. Mixing of the photon with low-mass particles. *Phys. Rev. D* **37**, 1237–1249 (1988).
12. Dessert, C., Long, A. J. & Safdi, B. R. X-ray signatures of axion conversion in magnetic white dwarf stars. *Phys. Rev. Lett.* **123**, 061104 (2019).
13. Tavecchio, F., Roncadelli, M. & Galanti, G. Photons to axion-like particles conversion in active galactic nuclei. *Phys. Lett. B* **744**, 375–379 (2015).
14. Brockway, J. W., Carlson, E. D. & Raffelt, G. G. SN 1987A gamma-ray limits on the conversion of pseudoscalars. *Phys. Lett. B* **383**, 439–443 (1996).
15. Csáki, C., Kaloper, N. & Terning, J. Dimming supernovae without cosmic acceleration. *Phys. Rev. Lett.* **88**, 161302 (2002).
16. Grossman, Y., Roy, S. & Zupan, J. Effects of initial axion production and photon-axion oscillation on type Ia supernova dimming. *Phys. Lett. B* **543**, 23–28 (2002).
17. Crnogorčević, M., Caputo, R., Meyer, M., Omodei, N. & Gustafsson, M. Searching for axionlike particles from core-collapse supernovae with Fermi LAT's low-energy technique. *Phys. Rev. D* **104**, 103001 (2021).
18. Conlon, J. P., Powell, A. J. & Marsh, M. C. D. Galaxy cluster thermal X-ray spectra constrain axionlike particles. *Phys. Rev. D* **93**, 123526 (2016).
19. Ajello, M. et al. Search for spectral irregularities due to photon–axionlike-particle oscillations with the Fermi Large Area Telescope. *Phys. Rev. Lett.* **116**, 161101 (2016).
20. Marsh, M. C. D. et al. A new bound on axion-like particles. *J. Cosmol. Astropart. Phys.* **12**, 036 (2017).
21. Reynolds, C. S. et al. Astrophysical limits on very light axion-like particles from Chandra grating spectroscopy of NGC 1275. *Astrophys. J.* **890**, 59 (2020).
22. Donnert, J., Vazza, F., Brüggen, M. & ZuHone, J. Magnetic field amplification in galaxy clusters and its simulation. *Space Sci. Rev.* **214**, 122 (2018).
23. Kachelriess, M. & Tjemsland, J. On the origin and the detection of characteristic axion wiggles in photon spectra. *J. Cosmol. Astropart. Phys.* **01**, 025 (2022).
24. Davies, J., Meyer, M. & Cotter, G. Constraints on axionlike particles from a combined analysis of three flaring Fermi flat-spectrum radio quasars. *Phys. Rev. D* **107**, 083027 (2023).
25. Cecil, R. & Meyer, M. Modeling the magnetic field of the Virgo cluster for axion like particle search in gamma ray energies. *Proc. Sci.* **417**, 182 (2023).
26. Hochmuth, K. A. & Sigl, G. Effects of axion-photon mixing on gamma-ray spectra from magnetized astrophysical sources. *Phys. Rev. D* **76**, 123011 (2007).
27. Wouters, D. & Brun, P. Constraints on axion-like particles from X-ray observations of the Hydra galaxy cluster. *Astrophys. J.* **772**, 44 (2013).
28. Conlon, J. P., Day, F., Jennings, N., Krippendorf, S. & Rummel, M. Constraints on axion-like particles from non-observation of spectral modulations for X-ray point sources. *J. Cosmol. Astropart. Phys.* **07**, 005 (2017).
29. Malyshev, D., Neronov, A., Semikoz, D., Santangelo, A. & Jochum, J. Improved limit on axion-like particles from gamma-ray data on Perseus cluster. Preprint at https://arxiv.org/abs/1805.04388 (2018).
30. Sisk-Reynés, J. et al. New constraints on light axion-like particles using Chandra transmission grating spectroscopy of the powerful cluster-hosted quasar H1821+643. *Mon. Not. R. Astron. Soc.* **510**, 1264–1277 (2022).
31. Matthews, J. H., Reynolds, C. S., Marsh, M. C. D., Sisk-Reynés, J. & Rodman, P. E. How do magnetic field models affect astrophysical limits on light axion-like particles? An X-ray case study with NGC 1275. *Astrophys. J.* **930**, 90 (2022).
32. Wouters, D. & Brun, P. Anisotropy test of the axion-like particle Universe opacity effect: a case for the Cherenkov Telescope Array. *J. Cosmol. Astropart. Phys.* **2014**, 016 (2014).
33. Jacobsen, S., Linden, T. & Freese, K. Constraining axion-like particles with HAWC observations of TeV blazars. *J. Cosmol. Astropart. Phys.* **10**, 009 (2023).
34. Abdollahi, S. et al. Incremental Fermi Large Area Telescope fourth source catalog. *Astrophys. J. Suppl. Ser.* **260**, 53 (2022).
35. Ballet, J., Bruel, P., Burnett, T. H., Lott, B. & The Fermi-LAT collaboration. Fermi Large Area Telescope fourth source catalog data release 4 (4FGL-DR4). Preprint at https://arxiv.org/abs/2307.12546 (2023).
36. Wen, Z. L., Han, J. L. & Yang, F. A catalogue of clusters of galaxies identified from all sky surveys of 2MASS, WISE, and SuperCOSMOS. *Mon. Not. R. Astron. Soc.* **475**, 343–352 (2018).
37. Planck Collaboration. Planck 2015 results. XXVII. The second Planck catalogue of Sunyaev-Zeldovich sources. *Astron. Astrophys.* **594**, A27 (2016).
38. Bulbul, E. et al. The SRG/eROSITA All-Sky Survey. The first catalog of galaxy clusters and groups in the Western Galactic Hemisphere. *Astron. Astrophys.* **685**, A106 (2024).
39. Sahakyan, N., Baghmanyan, V. & Zargaryan, D. Fermi-LAT observation of nonblazar AGNs. *Astron. Astrophys.* **614**, A6 (2018).
40. O'Hare, C. cajohare/AxionLimits: Axionlimits. *Zenodo* https://doi.org/10.5281/zenodo.3932430 (2020).
41. Nelson, D. et al. Introducing the TNG-Cluster simulation: overview and the physical properties of the gaseous intracluster medium. *Astron. Astrophys.* **686**, A157 (2024).
42. Dolag, K., Schindler, S., Govoni, F. & Feretti, L. Correlation of the magnetic field and the intra-cluster gas density in galaxy clusters. *Astron. Astrophys.* **378**, 777–786 (2001).
43. Govoni, F. et al. Sardinia Radio Telescope observations of Abell 194. The intra-cluster magnetic field power spectrum. *Astron. Astrophys.* **603**, A122 (2017).
44. Feretti, L., Giovannini, G., Govoni, F. & Murgia, M. Clusters of galaxies: observational properties of the diffuse radio emission. *Astron. Astrophys. Rev.* **20**, 54 (2012).
45. Steffen, F. D. Dark-matter candidates. Axions, neutralinos, gravitinos, and axinos. *Eur. Phys. J. C* **59**, 557–588 (2009).
46. Meyer, M., Horns, D. & Raue, M. First lower limits on the photon-axion-like particle coupling from very high energy gamma-ray observations. *Phys. Rev. D* **87**, 035027 (2013).

47. Giannotti, M., Irastorza, I., Redondo, J. & Ringwald, A. Cool WISPs for stellar cooling excesses. *J. Cosmol. Astropart. Phys.* **2016**, 057 (2016).
48. Ong, R. A., The CTA Consortium. Cherenkov Telescope Array: the next generation gamma-ray observatory. *Proc. Sci.* **ICRC2017**, 1071 (2018).
49. Gueta, O. The Cherenkov Telescope Array: layout, design and performance. *Proc. Sci.* **ICRC2021**, 885 (2022).
50. Merloni, A. et al. The SRG/eROSITA all-sky survey. First X-ray catalogues and data release of the western Galactic hemisphere. *Astron. Astrophys.* **682**, A34 (2024).
51. Norris, R. et al. The SKA Mid-frequency All-sky Continuum Survey: discovering the unexpected and transforming radio-astronomy. *Proc. Sci.* **AASKA14**, 86 (2015).
52. Loi, F. et al. Simulations of the polarized sky for the SKA: how to constrain intracluster magnetic fields. *Galaxies* **6**, 133 (2018).
53. Sikivie, P. Invisible axion search methods. *Rev. Mod. Phys.* **93**, 015004 (2021).
54. Mirizzi, A. & Montanino, D. Stochastic conversions of TeV photons into axion-like particles in extragalactic magnetic fields. *J. Cosmol. Astropart. Phys.* **2009**, 004 (2009).
55. Dobrynina, A., Kartavtsev, A. & Raffelt, G. Photon-photon dispersion of TeV gamma rays and its role for photon-ALP conversion. *Phys. Rev. D* **91**, 083003 (2015).
56. Mirizzi, A., Raffelt, G. G. & Serpico, P. D. in *Axions* (eds Kuster, M. et al.) 115–134 (Springer 2008).
57. Marsh, M. C. D., Matthews, J. H., Reynolds, C. & Carenza, P. Fourier formalism for relativistic axion-photon conversion with astrophysical applications. *Phys. Rev. D* **105**, 016013 (2022).
58. de Angelis, A., Mansutti, O. & Roncadelli, M. Axion-like particles, cosmic magnetic fields and gamma-ray astrophysics. *Phys. Lett. B* **659**, 847–855 (2008).
59. Matthews, J. ALPro: axion-like propagation. *Zenodo* https://doi.org/10.5281/zenodo.6137185 (2022).
60. Romano, P. et al. Prospects for gamma-ray observations of narrow-line Seyfert 1 galaxies with the Cherenkov Telescope Array. *Mon. Not. R. Astron. Soc.* **481**, 5046–5061 (2018).
61. Bonafede, A. et al. The Coma cluster magnetic field from Faraday rotation measures. *Astron. Astrophys.* **513**, A30 (2010).
62. Łokas, E. L. & Mamon, G. A. Dark matter distribution in the Coma cluster from galaxy kinematics: breaking the mass-anisotropy degeneracy. *Mon. Not. R. Astron. Soc.* **343**, 401–412 (2003).
63. Abe, K. et al. Prospects for γ-ray observations of the Perseus galaxy cluster with the Cherenkov Telescope Array. *J. Cosmol. Astropart. Phys.* **2024**, 004 (2024).
64. Kraljic, D., Rummel, M. & Conlon, J. P. ALP conversion and the soft X-ray excess in the outskirts of the Coma cluster. *J. Cosmol. Astropart. Phys.* **2015**, 011 (2015).
65. Kim, K. T., Kronberg, P. P., Giovannini, G. & Venturi, T. Discovery of intergalactic radio emission in the Coma-A1367 supercluster. *Nature* **341**, 720–723 (1989).
66. Stuardi, C. et al. The intracluster magnetic field in the double relic galaxy cluster Abell 2345. *Mon. Not. R. Astron. Soc.* **502**, 2518–2535 (2021).
67. Vacca, V. et al. The intracluster magnetic field power spectrum in A2199. *Astron. Astrophys.* **540**, A38 (2012).
68. Dupourqué, S. et al. CHEX-MATE: turbulence in the intra-cluster medium from X-ray surface brightness fluctuations. *Astron. Astrophys.* **687**, A58 (2024).
69. Bonafede, A. et al. Measurements and simulation of Faraday rotation across the Coma radio relic. *Mon. Not. R. Astron. Soc.* **433**, 3208 (2013).
70. Botteon, A., Brunetti, G. & Dallacasa, D. Constraining magnetic field strength in radio relics. *Proc. Sci.* **EXTRA-RADSUR2015**, 46 (2015).
71. Planck Collaborationet al. Planck intermediate results. X. Physics of the hot gas in the Coma cluster. *Astron. Astrophys.* **554**, A140 (2013).
72. Feretti, L. & Johnston-Hollitt, M. Magnetic fields in clusters of galaxies. *New Astron. Rev.* **48**, 1145–1150 (2004).
73. Govoni, F. et al. Rotation measures of radio sources in hot galaxy clusters. *Astron. Astrophys.* **522**, A105 (2010).
74. Finoguenov, A., Reiprich, T. H. & Boehringer, H. Details of the mass-temperature relation for clusters of galaxies. *Astron. Astrophys.* **368**, 749–759 (2001).
75. Osinga, E. et al. The detection of cluster magnetic fields via radio source depolarisation. *Astron. Astrophys.* **665**, A71 (2022).
76. Ajello, M. et al. The fourth catalog of active galactic nuclei detected by the Fermi Large Area Telescope: data release 3. *Astrophys. J. Suppl. Ser.* **263**, 24 (2022).
77. Pratt, G. W., Arnaud, M. & Pointecouteau, E. Structure and scaling of the entropy in nearby galaxy clusters. *Astron. Astrophys.* **446**, 429–438 (2006).
78. Zabalza, V. Naima: a Python package for inference of particle distribution properties from nonthermal spectra. *Proc. Sci.* **ICRC2015**, 922 (2016).
79. Domínguez, A. et al. Extragalactic background light inferred from AEGIS galaxy-SED-type fractions. *Mon. Not. R. Astron. Soc.* **410**, 2556–2578 (2011).
80. Feretti, L., Dallacasa, D., Giovannini, G. & Tagliani, A. The magnetic field in the Coma cluster. *Astron. Astrophys.* **302**, 680 (1995).
81. Taylor, G. B. et al. Magnetic fields in the centre of the Perseus cluster. *Mon. Not. R. Astron. Soc.* **368**, 1500–1506 (2006).
82. Lovisari, L. & Reiprich, T. H. The non-uniformity of galaxy cluster metallicity profiles. *Mon. Not. R. Astron. Soc.* **483**, 540–557 (2019).
83. Lidman, C. et al. Evidence for significant growth in the stellar mass of brightest cluster galaxies over the past 10 billion years. *Mon. Not. R. Astron. Soc.* **427**, 550–568 (2012).
84. Guidetti, D. et al. The intracluster magnetic field power spectrum in Abell 2382. *Astron. Astrophys.* **483**, 699–713 (2008).
85. Leahy, D. A. & Yin, D. X-ray analysis of the cluster 3C 129. *Mon. Not. R. Astron. Soc.* **313**, 617–626 (2000).
86. Taylor, G. B., Govoni, F., Allen, S. W. & Fabian, A. C. Magnetic fields in the 3C 129 cluster. *Mon. Not. R. Astron. Soc.* **326**, 2–10 (2001).
87. de Gasperin, F. et al. MeerKAT view of the diffuse radio sources in Abell 3667 and their interactions with the thermal plasma. *Astron. Astrophys.* **659**, A146 (2022).
88. Giacintucci, S. et al. Expanding the sample of radio minihalos in galaxy clusters. *Astrophys. J.* **880**, 70 (2019).
89. Lebeau, T., Sorce, J. G., Aghanim, N., Hernandez-Martinez, E. & Dolag, K. Mass bias in clusters of galaxies: projection effects on the case study of Virgo replica. *Astron. Astrophys.* **682**, A157 (2024).

Acknowledgements

We thank our colleagues D. R. Harvey, D. F. G. Fiorillo, J. U. Fynbo, M. Kachelrieß and M. Meyer for reading the draft of this paper and providing important comments that helped to improve the quality of this work. We greatly appreciate their insightful feedback and constructive suggestions. We acknowledge support from the state of Baden-Württemberg through bwHPC. L.Z.'s work is supported by a Scholars at Risk Denmark Fellowship for Scholars from Ukrainian Universities (SARU Fellowship) at the University of Copenhagen. This project has received funding through the MSCA4Ukraine project (Grant No 1.4-UKR-1245772-MSCA4Ukraine), which is funded by the European Union. The views and opinions expressed are, however, those of the authors only and do not necessarily reflect those of the European Union, the European Research Executive Agency or the MSCA4Ukraine Consortium. The European Union, the European Research Executive Agency and the MSCA4Ukraine Consortium as a whole or any individual member institutions of the MSCA4Ukraine Consortium cannot be held responsible for them. This research was conducted with support from the Centre for the Collective Use of Scientific Equipment in the Laboratory of High Energy Physics and Astrophysics of Taras Shevchenko National University of Kyiv.

Author contributions

D.M. performed the data analysis. D.M., L.Z. and O.R. interpreted the results and drafted the paper. Y.B. adapted the ALPro code for the analysis and generated samples of both individual and averaged absorption features. A.S. contributed to the definition of the project scope and provided comments on the paper. All authors contributed to the writing, reviewed the paper, and discussed and provided feedback on the results.

Competing interests

The authors declare no competing interests.

Additional information

Extended data is available for this paper at https://doi.org/10.1038/s41550-025-02621-8.

Supplementary information The online version contains supplementary material available at https://doi.org/10.1038/s41550-025-02621-8.

Correspondence and requests for materials should be addressed to Denys Malyshev or Oleg Ruchayskiy.

Peer review information *Nature Astronomy* thanks Francesca Chadha-Day, Manuel Meyer and the other, anonymous, reviewer(s) for their contribution to the peer review of this work.

https://doi.org/10.1038/s41550-025-02621-8

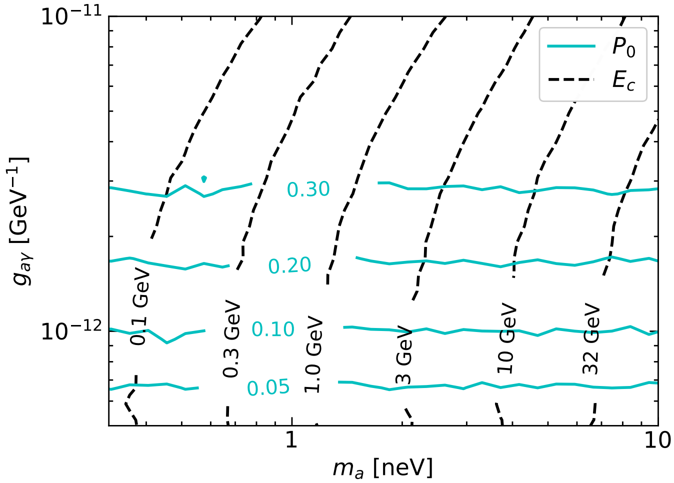

Extended Data Fig. 1 | Dependence of the averaged photon survival probability function's shape parameters on ALP parameters. Dependence of the shape parameters E_c and p_0, as defined by Equation (2), on the ALP parameters (m_a, $g_{a\gamma}$) for the range of parameters considered in this work. The parameter k is normally distributed with the mean 2.71 and the standard deviation 0.33.

https://doi.org/10.1038/s41550-025-02621-8

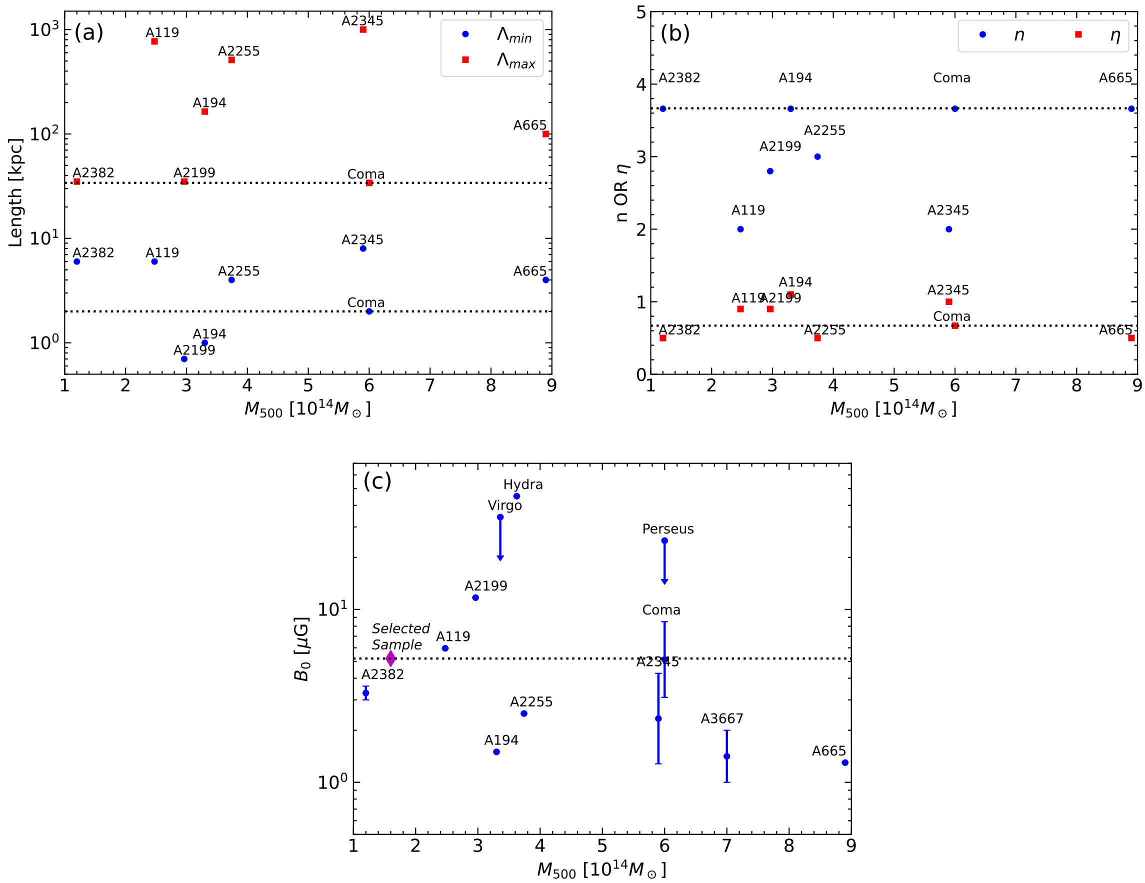

Extended Data Fig. 2 | Properties of the magnetic fields across the samples of galaxy clusters. Panel (**a**) illustrates the coherence lengths of magnetic fields. The minimal coherence lengths (Λ_{min}) are represented by blue circles, while the maximum coherence lengths (Λ_{max}) are denoted by red squares. Panel (**b**) presents the magnetic field power spectrum index, n (blue circles), while red squares represent the index η as defined in Equation (11). Panel (**c**) displays the central magnetic field strength (B_0). Error bars indicate the measurement uncertainties (from minimal to maximal value reported in the literature) of B_0, and arrows signify upper limits on the magnetic field measurements. Horizontal lines in all panels represent the parameter values adopted in this study. The data points for individual galaxy clusters are derived from refs. 25,43,62,67,73,80–89.

https://doi.org/10.1038/s41550-025-02621-8

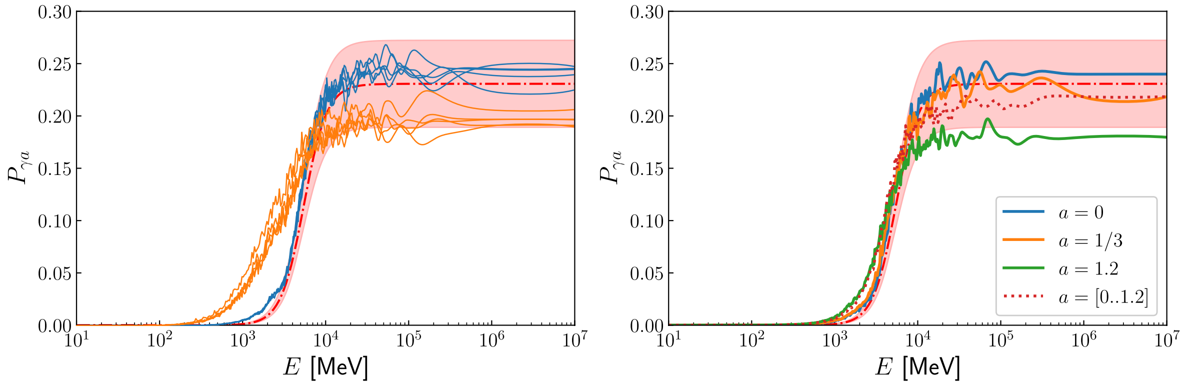

Extended Data Fig. 3 | Dependence of the photon-to-ALP conversion probability on assumed magnetic field properties. *Left panel:* Average conversion probability over 32 realizations for the Coma cluster (**blue lines**) and Coma-like clusters (**orange lines**). For the blue curves, each realization varies the magnetic field direction and domain size distribution while maintaining a fixed radial profile (Equation (11)) with magnetic field and electron density values matching those of the Coma cluster. For the orange curves, the central magnetic field amplitude, B_0, is also varied, sampled from a log-uniform distribution (0.52 to 52 μG), resulting in a ~ 20% change in the average absorption feature. *Right panel:* Sensitivity of the results to the parameter a, which governs the domain size distribution as a proxy for the turbulent magnetic field power spectrum slope. The nominal value $a = 1/3$ corresponds to the Kolmogorov turbulence spectrum. Allowing variation in a results in the dotted line, which remains within the uncertainty range. In both panels, the red dashed-dotted curve represents $1 - P_{\gamma\gamma}$, where $P_{\gamma\gamma}$ is given by Equation (2) with nominal values of p_0, E_c, and k corresponding to the ALP parameters $(m_a, g_{a\gamma}) = (3\,\text{neV}, 2 \times 10^{-12}\,\text{GeV}^{-1})$. The red shaded region indicates a ± 20% systematic uncertainty, accounting for corrections due to the finite size of our sample. Domain sizes vary randomly between $\Lambda_{\min} = 2$ kpc and $\Lambda_{\max} = 34$ kpc.

https://doi.org/10.1038/s41550-025-02621-8

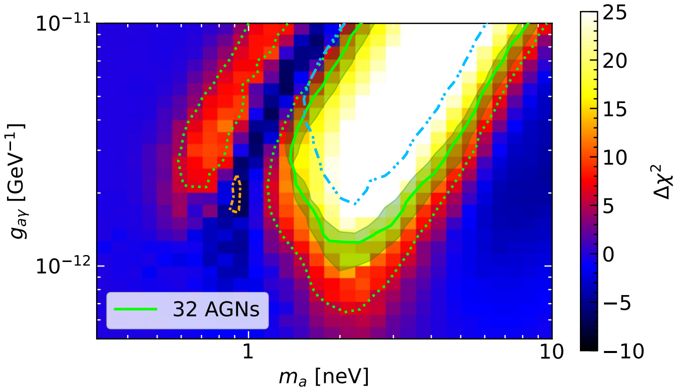

Extended Data Fig. 4 | χ^2 change and ALP exclusion regions. The colors illustrate the change in χ^2 between the baseline and the ALP models for the combined fit of 32 AGNs, assuming statistical-only uncertainties. The green contours represent 2σ-excluded regions ($\Delta\chi^2 = 6.2$ for 2 d.o.f.) for two different treatments of the systematic uncertainties. Dotted and solid lines correspond to the zero (that is, statistical only) and nominal levels of *Fermi/LAT* data systematic uncertainties. The shaded region shows the uncertainty related to the magnetic field estimation in the Coma cluster. The dash-dot-dotted region illustrates the weakening of the limits for the maximally conservative choice of the magnetic field in the selected sample of galaxies (for the nominal level of *Fermi/LAT* systematics). The dash-dotted orange region corresponds to a 2σ detection region where the ALP model actually improves $\Delta\chi^2$ by at least 6.2.

https://doi.org/10.1038/s41550-025-02621-8

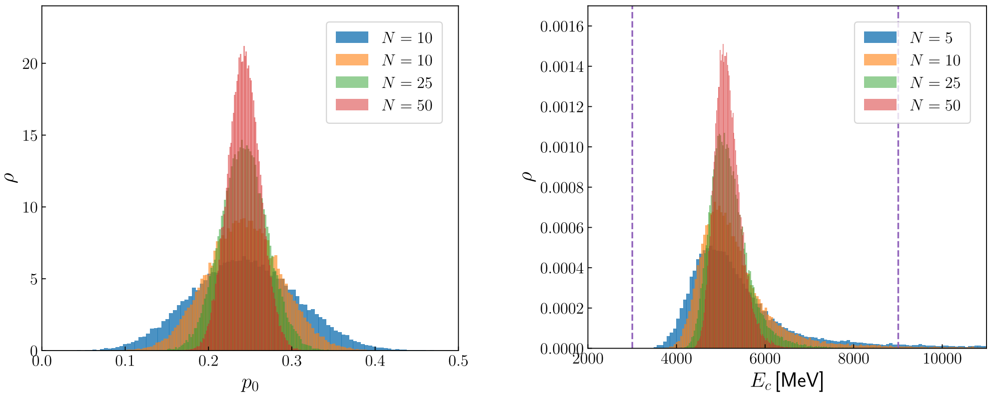

Extended Data Fig. 5 | Corrections to the parameters of the ALP model due to the finite *N*. *Left panel*: The probability density of finding a given value of p_0 as a function of the number of realizations. The width of the distribution for $N = 25$ is 20%. *Right panel*: the same but for the characteristic energy E_c. The width of the distribution for $N = 25$ is 12%. Vertical lines indicate the size of the *Fermi/LAT* energy bin, showing that the scatter of values lies well within the bin size. All results correspond to $(m_a, g_{a\gamma}) = (3\,\mathrm{neV}, 2\times10^{-12}\mathrm{GeV}^{-1})$.

https://doi.org/10.1038/s41550-025-02621-8

Extended Data Table 1 | List of *Fermi/LAT* AGNs located behind/within galaxy clusters

Fermi/LAT source	$z_{\rm AGN}$	Cluster	$z_{\rm GC}$	D (kpc)	M_{500} $(10^{14}M_\odot)$	Reference
4FGL J0014.2+0854	0.163	J001419.7+085401	0.159	192.8	2.9	T1 [36]
4FGL J0038.2-2459	1.196	J003757.6-250425	0.064	478.8	1.9	T1 [36]
4FGL J0049.0+2252	0.264	J004857.8+225427	0.151	392.3	1.1	T1 [36]
4FGL J0132.7-0804	0.148	J013241.2-080405	0.136	130.0	2.4	T1,T3 [36]
4FGL J0317.8-4414	0.076	J031757.7-441418	0.061	58.4	3.0	T1,T3,P1 [36,37]
4FGL J0617.7-1715	0.098	J061733.4-171525	0.093	237.1	2.8	T1 [36]
4FGL J0912.5+1556	0.212	J091230.5+155658	0.196	254.5	1.1	T1 [36]
4FGL J0914.4+0249	0.427	J091428.2+025036	0.160	141.2	2.0	T1 [36]
4FGL J1010.8-0158	0.896	J101056.5-015927	0.196	463.8	4.3	T1 [36]
4FGL J1013.7+3444	0.208	J101350.8+344251	0.143	277.9	2.3	T1 [36]
4FGL J1058.4+0133	0.890	J105811.0+013617	0.038	254.1	2.0	T1,T3, E1 [36,38]
4FGL J1202.5+3852	0.805	J120230.5+385219	0.283	350.9	1.1	T1 [36]
4FGL J1213.0+5129	0.796	J121246.7+513250	0.084	467.4	0.9	T1 [36]
4FGL J1303.0+2434	0.993	J130303.4+243456	0.295	135.0	2.6	T1 [36]
4FGL J1353.2+3740	0.216	J135314.1+374114,	0.216	95.1	1.8	T1 [36]
		J135318.5+373838	0.094	291.7	1.9	T1 [36]
4FGL J1508.8+2708	0.270	J150843.1+271046	0.081	269.7	1.4	T1 [36]
4FGL J1516.8+2918	0.130	J151641.6+291809	0.130	339.6	1.2	T1,T3 [36]
4FGL J1615.6+4712	0.199	J161541.3+471004	0.198	498.5	2.3	T1 [36]
4FGL J2041.9-3735	0.099	J204154.9-373849	0.093	413.9	1.2	T1 [36]
4FGL J2314.0+1445	0.164	J231357.4+144423	0.143	237.9	2.2	T1 [36]
4FGL J2321.9+2734	1.253	J232159.1+273443	0.093	53.0	1.9	T1,T3 [36]
4FGL J2336.6+2356	0.127	J233642.1+235529	0.105	205.0	2.3	T1,T3 [36]
4FGL J2338.9+2124	0.291	J233853.3+212753	0.071	326.3	1.3	T1 [36]
4FGL J0303.3-7913	1.115	J030351.6-791228	0.189	383.8	0.3	T2 [36]
4FGL J0309.4-4000	0.193	J030937.3-400045	0.141	353.4	0.2	T2 [36]
4FGL J0654.4+4514	0.928	J065427.7+451447	0.374	174.7	0.6	T2 [36]
4FGL J1242.9+7315	0.075	J124311.3+731559	0.074	87.7	0.3	T2 [36]
4FGL J1144.9+1937	0.022	PSZ2 G234.59+73.01	0.021	478.6	1.67	P1[37]
4FGL J0805.2-0110	1.388	1eRASS J080515.1-011145	0.095	137.6	1.65	E1[38]
4FGL J1116.6+2915	0.047	1eRASS J111634.6+291527	0.047	55.1	1.02	E1[38]
4FGL J0319.8+4130	0.017559	Perseus	0.017559	–	6.1	NED[88]
4FGL J1230.8+1223	0.004283	Virgo	0.004283	–	3.36	NED[89]

The table summarizes the names of AGNs as presented in the 4FGL *Fermi/LAT* catalog, their redshifts z_{agn}, corresponding clusters, and their redshifts z_{gc}. The comoving distance at the redshift of the cluster, corresponding to the angular separation between the AGN and the cluster's center, is given by *D*. The M_{500} of the clusters[36] is estimated as $M_{500} \sim 0.5 \times 10^{14} M_\odot (R_{L*}/8.0)^{1.08}$. The reference column specifies the source from which the clusters' data were adopted.

 https://doi.org/10.1038/s41550-025-02621-8

Extended Data Table 2 | Best-fit χ^2 of the models fitting *Fermi/LAT* AGNs

Fermi/LAT source	Average significance	χ_0^2	χ_{ALP}^2	$\Delta\chi^2$
4FGL J0014.2+0854	5.97	2.04	2.22	0.18
4FGL J0038.2-2459	97.56	16.03	13.73	-2.30
4FGL J0049.0+2252	8.03	0.99	0.97	-0.02
4FGL J0132.7-0804	9.97	2.16	2.24	0.08
4FGL J0317.8-4414	5.78	1.64	1.56	-0.09
4FGL J0617.7-1715	29.06	4.89	3.84	-1.05
4FGL J0912.5+1556	12.90	3.02	3.08	0.06
4FGL J0914.4+0249	6.56	1.35	1.20	-0.15
4FGL J1010.8-0158	9.64	1.90	1.98	0.08
4FGL J1013.7+3444	20.74	5.06	5.43	0.36
4FGL J1058.4+0133	102.24	2.88	3.18	0.30
4FGL J1202.5+3852	10.22	1.82	1.86	0.03
4FGL J1213.0+5129	16.84	4.72	4.49	-0.23
4FGL J1303.0+2434	53.97	2.07	1.52	-0.54
4FGL J1353.2+3740	9.85	2.71	2.56	-0.14
4FGL J1508.8+2708	12.74	0.81	0.76	-0.05
4FGL J1516.8+2918	7.66	1.36	1.31	-0.05
4FGL J1615.6+4712	20.86	2.86	2.42	-0.44
4FGL J2041.9-3735	14.21	0.94	0.96	0.02
4FGL J2314.0+1445	22.79	4.78	4.72	-0.06
4FGL J2321.9+2734	36.10	4.85	4.92	0.07
4FGL J2336.6+2356	12.05	5.92	5.80	-0.13
4FGL J2338.9+2124	17.84	1.17	1.53	0.36
4FGL J0303.3-7913	10.82	3.75	3.49	-0.26
4FGL J0309.4-4000	7.53	0.89	1.05	0.16
4FGL J0654.4+4514	36.34	3.64	3.64	0.01
4FGL J1242.9+7315	12.31	7.80	7.97	0.16
4FGL J0319.8+4130	251.54	7.59	2.81	-4.78
4FGL J1230.8+1223	46.98	9.73	10.79	1.06
4FGL J1144.9+1937	14.79	4.51	5.10	0.58
4FGL J0805.2-0110	19.37	3.21	2.97	-0.24
4FGL J1116.6+2915	3.80	1.44	1.40	-0.05
Total	–	118.54	111.47	-7.07

A summary of the best-fit χ^2 of the models fitting the spectra of selected *Fermi/LAT* sources with (χ^2_{ALP}) and without (χ^2_0) ALP components; see the text for more details. The mass and coupling constant of the ALP were selected to match the parameters of the marginal 2σ detection ($m_a = 9.1 \times 10^{-10}$ eV, $g_{a\gamma} = 2.1 \times 10^{-12}$ GeV^{-1}). The negative $\Delta\chi^2 = \chi^2_{\mathrm{ALP}} - \chi^2_0$ indicates an improvement of the ALP-invoking model compared to the baseline fit model. The "Average significance" column indicates the average significance of the given source according to the 4FGL catalog.